



# Reduced reference image quality assessment using regularity of phase congruency<sup>☆</sup>



Delei Liu<sup>a</sup>, Yong Xu<sup>a,\*</sup>, Yuhui Quan<sup>a</sup>, Patrick Le Callet<sup>b,1</sup>

<sup>a</sup> School of Computer Science & Engineering, South China University of Technology, Guangzhou 510006, China

<sup>b</sup> IRCCyN Lab, University of Nantes, BP 50609 44306 Nantes Cedex 3, France

## ARTICLE INFO

### Article history:

Received 21 November 2013

Received in revised form

15 June 2014

Accepted 15 June 2014

Available online 23 June 2014

### Keywords:

Reduced-reference image quality assessment

Fractal dimension

Phase congruency

## ABSTRACT

In this paper, a reduced-reference image quality assessment metric is proposed, which measures the difference of the regularity of the phase congruency (PC) between the reference image and the distorted image. The proposed model adopts a three-stage approach. The PC of the image is first extracted, then the fractal dimensions are computed on PC as the image features that characterize the image structures from the view of the spatial distribution. Finally the image features are pooled as the quality score using  $\ell_1$  distance. The proposed approach is evaluated on seven public benchmark databases. Experimental results have demonstrated the excellent performance of the proposed approach.

© 2014 Elsevier B.V. All rights reserved.

## 1. Introduction

The quality of digital images is rarely perfect. Images are subject to distortions during acquisition, compression, transmission, processing, and reproduction. To maintain, control, and enhance the quality of images, it is important for image acquisition, management, communication, and processing systems to be able to identify and quantify image quality degradations. The development of effective automatic image quality assessment systems is a necessary goal for this purpose.

Image quality assessment (IQA) methods can be categorized into subjective and objective methods [1].

Subjective IQA directly gives image quality by human subjects. This method, though reliable, is expensive and too slow for real-world applications. So objective IQA has been desired, where the goal is to provide computational models that can automatically predict perceptual image quality.

According to the availability of a reference image, objective IQA metrics can be classified as full reference (FR), no-reference (NR) and reduced-reference (RR) methods. FR-IQA [2–6] requires full access to an original reference image that is assumed to have perfect quality. However, in many practical applications, an IQA system does not have access to the reference image. Blind/NR-IQA [7–9] turns out to be a very difficult task, due to the varied image contents and the individual distortion types, although human observers usually can effectively and reliably assess the quality of distorted images without using any reference at all. RR-IQA [10–14] strikes the balance of FR-IQA and NR-IQA and it predicts the quality degradation of an image with only partial information about the reference image. In this paper, the discussion is confined to RR-IQA methods.

<sup>☆</sup> Project supported by National Nature Science Foundations of China (61273255, 61211130308 and 61070091), Fundamental Research Funds for the Central Universities (SCUT 2013ZG0011) and Guangdong Technological innovation project (2013KJCX0010).

\* Corresponding author.

E-mail addresses: [liu.dl@mail.scut.edu.cn](mailto:liu.dl@mail.scut.edu.cn) (D. Liu), [yxu@scut.edu.cn](mailto:yxu@scut.edu.cn) (Y. Xu), [yuhui.quan@mail.scut.edu.cn](mailto:yuhui.quan@mail.scut.edu.cn) (Y. Quan), [patrick.lecallet@univ-nantes.fr](mailto:patrick.lecallet@univ-nantes.fr) (P.L. Callet).

<sup>1</sup> EURASIP membership.

As we know, on the way to RR-IQA metric, the key issue is feature detection and extraction. Therefore, studying and exploiting the special properties of natural images has been one of the most important tasks in RR-IQA. The current research either depends on some statistic models of natural images (e.g., [12,14–16]) or relies on the histogram of local patterns in some transform domain (e.g., [10,17,18]). All of these methods lose the image spatial information and cannot explicitly represent the image structural information. Although the change of the number of image elements is certainly related to the varying of image quality, it is insufficient to characterize the perception of human visual system (HVS) to visual quality.

Motivated by the evidence presented in [19–23] that visually discernable features coincide with those points where the Fourier waves at different frequencies have congruent phases, and the power law relationship for PC, which can be characterized well by fractal analysis. In this paper, we propose a new approach to RR-IQA based on PC and fractal analysis.

The proposed approach, called Similarity of PC Regularity (SPCR), characterizes the regularity of the PC. The PC of the image is first extracted. Then the PC is characterized by fractal dimension as the image features. Finally these image features are pooled as the quality score by computing  $\ell_1$  distance between the features of the reference image and that of the distorted one. In our implementation, we have two versions of SPCR that defined on the intensity image and the partial gradient image respectively. Our approach is evaluated on seven famous benchmark IQA databases using five popular evaluation metrics. The competitive results achieved demonstrate that our method performs on par with the state-of-the-art approaches.

Actually, PC has already been used for IQA in the literature and has shown its power in several quality assessment studies [6,24–27]. In [6,24,25], PC is used for FR-IQA; In [26,27], PC is employed for NR-IQA. PC will be used in the RR-IQA in this paper.

The rest of this paper is organized as follows: Section 2 is devoted to related work. Section 3 gives a brief review on PC and fractal analysis, A detailed description of our proposed metric is given in Section 4. Experimental results and analysis are presented in Section 5. Finally, Section 6 concludes the paper.

## 2. Related work

In recent years, a number of RR-IQA methods have been developed, we give a brief review in this section.

In previous work, RR-IQA focuses on the specific types of image distortions, these methods use image distortion modeling [18,28] developed for specific application environments. For instance, in [28], a hybrid image quality metric combines five structural features: blocking, blur, edge-based image activity, gradient-based image activity and intensity masking. The metric makes a similarity assessment between the distorted image and the reference image to assess JPEG coded images. However, these metrics suffer from bad performance when images with different distortion types are tested together, because the models are built for each distortion type respectively.

Recent work has concentrated on general-purpose RR-IQA methods. These approaches are mostly based on natural image statistical model [12,14,15,17] and have achieved impressive results in RR-IQA. The basic idea of these methods is to quantify the image quality by quantifying the disturbance to the image statistics caused by the distortion. Wang et al. [14] modeled natural images using the marginal probability distributions of the coefficients in wavelet domain, and the Kullback–Leibler distance (KLD) between two marginal distributions is used to measure the image distortion. In order to model the perceptual sensitivity of biological vision, Li et al. [12] proposed the so-called divisive normalization transformation (DNT) for image representation. The image statistic is based on the Gaussian scale mixtures (GSM) model and the KLD is used to pool the features to the final score. In [10], according to the distribution of wavelet coefficients, geometric information is extracted for quality assessment. In [16], the generalized Gaussian density is employed to model the distribution of the discrete cosine transform (DCT) coefficients. Xue et al. [15] employed the Weibull distribution to describe the statistics of image gradient magnitude. In [13], the image quality is measured by the difference between the entropies of wavelet coefficients of reference and distorted images. To adapt the SSIM [29] to RR-IQA, Rehman et al. [2] combined the GSM-based statistics in a multi-scale and multi-orientation DNT domain following the philosophy in the construction of SSIM. A regression-by-discretization method is then applied to normalize the measure across image distortion types. All of these methods are based on counting the difference of the numbers of elements in two images, which lose the details of how the elements are distributed.

Compared with statistical approaches, fractal dimension can encode spatial information in the form of geometrical distribution of the point sets [30]. Moreover, it is well known that phase information provides the most significant information within an image [31], and the PC is coincide with the visually discernable features [19–23]. More recently, PC has successfully been used for FR-IQA [6,24–27] and NR-IQA [6,24,25]. However, how to encode phase information for RR-IQA is a challenge problem, to this end, in this paper we attempt to incorporate PC and fractal analysis into the design of RR-IQA.

## 3. Preliminaries

Before presenting the detailed description of our approach, we first give an introduction of two mathematical tools upon which our approach is built. We first describe the definition of PC. Then we introduce fractal dimension which encodes PC, which offers us the ability to precisely evaluate the visual information of images.

### 3.1. Phase congruency

PC is first defined in [21] in terms of the fourier series expansion of a signal at location  $x$ :

$$PC(x) = \max_{\theta \in [0, 2\pi]} \frac{\sum_n A_n \cos(\Phi_n(x) - \overline{\Phi(x)})}{\sum_n A_n}, \quad (1)$$

where  $A_n$  is the amplitude of  $n$ th Fourier component, and  $\Phi_n(x)$  is the local phase of Fourier component, and  $\bar{\Phi}(x)$  is the mean average local phase. It should be noted that PC is a real number within  $0 \sim 1$ . If all the Fourier components are in the same phase at location  $x$ ,  $PC(x)$  would be 1. If there is no coherence of phase,  $PC(x)$  falls to a minimum of 0. PC provides a measure that is independent of the overall magnitude of the signal making it invariant to variations in image illumination and/or contrast.

PC is further modified and extended to two dimensions via the 2D log-Gabor filters by Kovsi [32]. The Log-Gabor filters are defined in the frequency domain using polar coordinates by the transfer function  $H(f, \theta)$  constructed as a following product:

$$H(f, \theta) = H_f \cdot H_\theta, \quad (2)$$

the radial component  $H_f$  controlling the bandwidth that the filter responds to, and the angular component  $H_\theta$  controlling the spatial orientation that the filter responds to. The 2D Log-Gabor filters can be represented in a polar form as

$$H(f, \theta) = \exp \left[ -\frac{[\log(f/f_0)]^2}{[2\log(\sigma_f/f_0)]^2} \right] \cdot \exp \left[ -\frac{(\theta - \theta_0)^2}{2\sigma_\theta} \right], \quad (3)$$

where  $f_0$  is the filter's center frequency, and  $\theta_0$  the filter's direction. To obtain constant shape ratio filters, the term  $\sigma_f/f_0$  must also be held constant for varying  $f_0$ .

By modulating  $f_0$  and  $\theta_j$  and convolving with the image, we get a set of responses at each point  $x$  as  $[e_{n,\theta_j}(x), o_{n,\theta_j}(x)]$ . The local amplitude on scale  $n$  and orientation  $\theta_j$  is  $A_{n,\theta_j}(x) = \sqrt{e_{n,\theta_j}(x)^2 + o_{n,\theta_j}(x)^2}$ , and the local along orientation  $\theta_j$  is  $E_{\theta_j}(x) = \sqrt{F_{\theta_j}(x)^2 + H_{\theta_j}(x)^2}$ , where  $F_{\theta_j}(x) = \sum_n e_{n,\theta_j}(x)$  and  $H_{\theta_j}(x) = \sum_n o_{n,\theta_j}(x)$ . The 2D PC at  $x$  is defined as

$$PC(x) = \frac{\sum_j E_{\theta_j}(x)}{\sum_n \sum_j A_{n,\theta_j}(x) + \varepsilon}, \quad (4)$$

where  $\varepsilon$  is a positive constant ensuring the numerical stability.

In this work, the major reason to adopt the PC is that visually discernable features of images coincide with PC [19–23], which provides convenience for further feature extraction.

### 3.2. Fractal analysis

Fractal analysis is introduced and developed by Mandelbrot [33] as a means for describing and analyzing the properties of objects with irregular and complex structure in nature. The characteristic property of fractals can be viewed as the objects with statistical self-similarity. The numerical quantification of self-similarity is obtained by the fractal dimension. The fractal dimension  $d$  is a measure of a given point set  $E$  in a certain measurement space  $m(\cdot)$  by measuring its power law behavior with respect to the scale  $\delta$ :

$$m_\delta(E) \propto \delta^{-d},$$

where  $m_\delta(E)$  is some measurement of the given point set  $E$  at

scale  $\delta$ . For images, the measurement could be intensity, PC, etc.

There are many techniques to estimate the fractal dimension of image surface. One popular approach is the so-called *differential box counting* (DBC) method, which has the advantage of efficiency, accuracy and generality [34]. The DBC method considers an image  $I(x, y)$  of size  $M \times M$  as a 3D point set  $\{(x, y, z) | z = I(x, y)\}$ , where  $(x, y)$  denotes the 2D position and  $z$  denotes the gray level of the image. Suppose the image is scaled down to a size  $s \times s$ , where  $s$  is an integer and  $1 < s \leq M/2$ . Let  $r = s/M$ . The  $(x, y)$  space is partitioned into grids of size  $s \times s$ . A column of boxes of size  $s \times s \times h$  are placed on each grid respectively, where  $h$  denotes the height of a single box. We generally set the values of  $h$  and  $s$  to satisfy  $G/h = M/s$ , where  $G$  is the total number of gray levels. Suppose the minimum gray value and the maximum gray value in the  $(i, j)$ th grid fall in the  $k$ th box and the  $l$ th box respectively, we compute the contribution  $n_r(i, j)$  in the  $(i, j)$ th grid as follows:

$$n_r(i, j) = l - k + 1. \quad (5)$$

Summing contributions from all grids, we have

$$N_r = \sum_{ij} n_r(i, j), \quad (6)$$

where  $N_r$  is counted for different values of  $r$ . Then the DBC fractal dimension is defined as

$$d_{DBC} = \lim_{r \rightarrow 0} \frac{\log(N_r)}{-\log r}. \quad (7)$$

In practice,  $d_{DBC}$  can be estimated from the least squares linear fitting in the  $\log(N_r) - \log(1/r)$  coordinates system.

It is noted that there are many other techniques to estimate the fractal dimension of image surface, such as “interpolation method” [35] and MLE [36] et al. We found that the final results using different methods are almost similar to image quality assessment. The reason that we select DBC is that it is simple, quick and achieves satisfactory result.

In this work, fractal analysis is adopted to encode the PC. The advantages of employed fractal analysis are as follows:

First, fractal dimension has a strong correlation with HVS [37]. Second, compared with statistical approaches, fractal dimension can encode spatial information in the form of geometrical distribution of the point sets [30].

As we known, intensity images of most natural surfaces are isotropic fractals [37]. To demonstrate that PC of the image can also be characterized by the fractal model, we plot the behaviors of PC by log–log fitting in Fig. 1. It can be seen that the PC do behave according to some power law.

### 4. Similarity of PC regularity

In this section, we present the proposed SPQR approach. The outline of our approach is illustrated in Fig. 2. There are two stages in our approach. In the first stage, the image features based on fractal analysis are computed. In the second stage, the features are pooled into

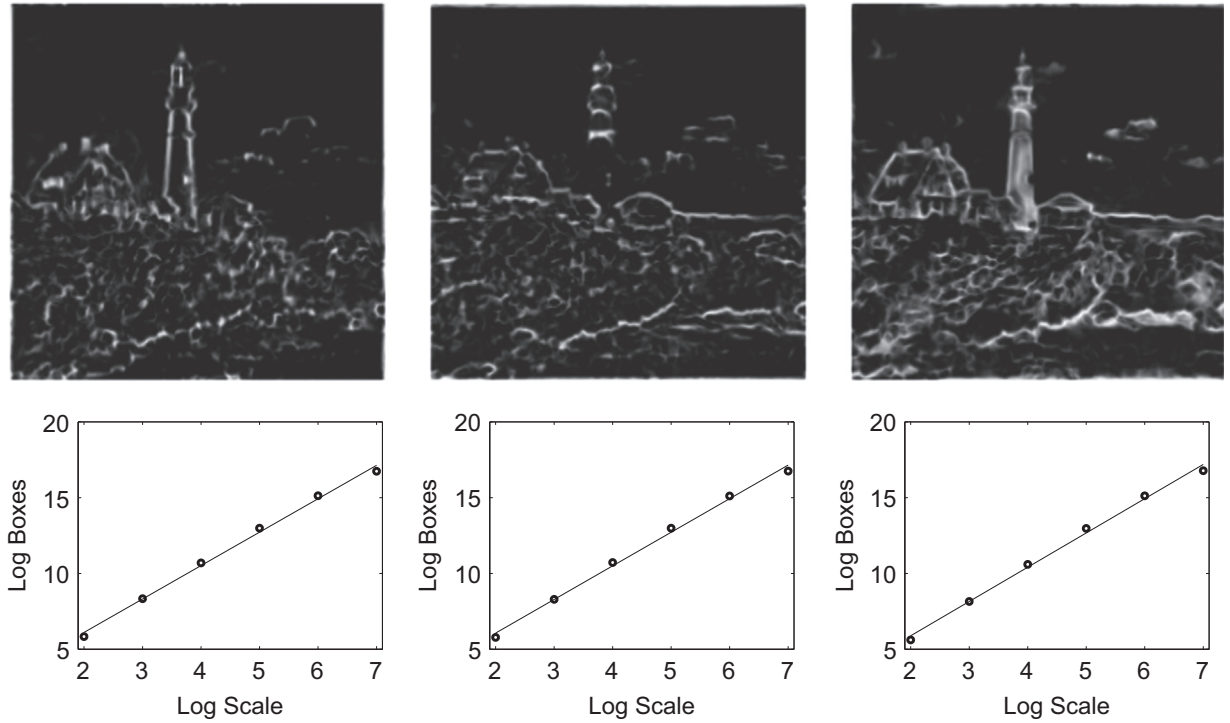


**Fig. 1.** Log–log plot of box number versus box scale for PC. The upper row shows the PC of the reference image in Fig. 3 (with horizontal, vertical derivative domain and intensity domain). The bottom row shows the corresponding log–log fittings.

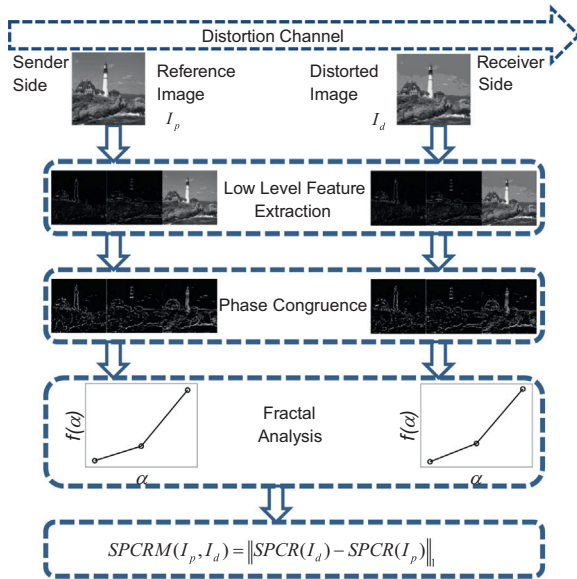


**Fig. 2.** Illustration for the SPCR index computation.

a single index measure using  $\ell_1$  distance. In the rest of this section, we will give the details of each stage.

#### 4.1. Feature extraction based on fractal analysis

Given an image  $I$ , we first compute some measurement  $m(\cdot)$  on  $I$  to extract the low-level vision features  $m(I)$ . The

**Table 1**  
Partial derivatives of  $f(x)$  using operators.

Operator	$\nabla_x$	$\nabla_y$
Scharr	$\frac{1}{16} \begin{bmatrix} 3 & 0 & -3 \\ 10 & 0 & -10 \\ 3 & 0 & -3 \end{bmatrix} * f(x)$	$\frac{1}{16} \begin{bmatrix} 3 & 10 & 3 \\ 0 & 0 & 0 \\ -3 & -10 & -3 \end{bmatrix} * f(x)$
Sobel	$\frac{1}{4} \begin{bmatrix} 1 & 0 & -1 \\ 2 & 0 & -2 \\ 1 & 0 & -1 \end{bmatrix} * f(x)$	$\frac{1}{4} \begin{bmatrix} 1 & 2 & 1 \\ 0 & 0 & 0 \\ -1 & -2 & -1 \end{bmatrix} * f(x)$
Prewitt	$\frac{1}{3} \begin{bmatrix} 1 & 0 & -1 \\ 1 & 0 & -1 \\ 1 & 0 & -1 \end{bmatrix} * f(x)$	$\frac{1}{3} \begin{bmatrix} 1 & 1 & 1 \\ 0 & 0 & 0 \\ -1 & -1 & -1 \end{bmatrix} * f(x)$

measurement can be the intensity measurement  $m_{int}$ , the gradient measurement  $m_{grad}$  that are defined as follows:

$$m_{int}(I) = I, \quad (8)$$

$$m_{grad}(I) = \nabla I, \quad (9)$$

where  $\nabla$  is the partial derivative operator (here we adopt the Scharr gradient operator listed in Table 1. By using other operators such as the Sobel and Prewitt operators, the proposed method will have similar results). By using these two measurements, our approach can capture different structures of natural images from different aspects. In practice, using image gradient to design IQA models [6,38–40] is popular since it can effectively capture image local structures, to which the HVS is highly sensitive. The most commonly encountered image distortions, such





**Fig. 3.** Reference image and five distorted images with different types of distortion in the LIVE dataset (JPEG2000, JPEG, WHITE NOISE, GBLUR, FAST FADDING respectively).

as noise corruption, blur and compression artifacts, will lead to highly visible structural changes in the gradient domain.

Next, in order to capture the visually discernable features, PC is run on  $m(I)$ , resulting in PC on image intensity domain and partial derivative domain. Finally, we extract features from the PC via fractal analysis. In our implementation, we compute the DBC fractal dimension on each PC using (7) denoted by SPCR(including  $SPCR_{int}$  and  $SPCR_{scharr}$ ) as follows,

$$SPCR_{int}(I) = \{d_{DBC}(PC_I(m(I)))\}, \quad (10)$$

$$SPCR_{scharr}(I) = \{d_{DBC}(PC_{\nabla_x}(m(I))), d_{DBC}(PC_{\nabla_y}(m(I)))\}. \quad (11)$$

As we known, features used by RR-IQA should be sensitive to various image distortions. Fig. 3 shows a reference image and five distorted images with different types of distortion in the LIVE database [41], and their corresponding SPCR features are demonstrated in Fig. 4. One can see that the different types of distortions result in the different SPCR. Thus, SPCR can reflect the global changes of the image structures caused by different types of distortion, but its ability is limited to reflect the local distortion. Hence, we modify our SPCR method to adapt the local distortion case as follows. A given image is first divided into non-overlapped sub-images, and then the original SPCR features are computed on each subimage and concatenated as output. In other words, the modified SPCR features are defined as

$$SPCR_{int}(I) = \bigcup_i d_{DBC}(P_i(PC_{intensity}(m(I)))), \quad (12)$$

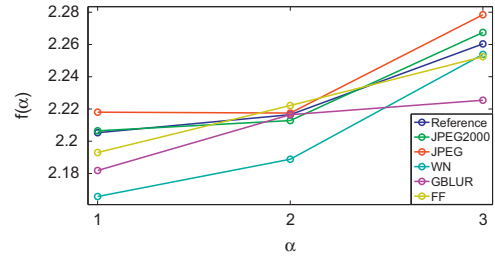


**Fig. 4.** The SPCR features of the images shown in Fig. 3. The variable  $\alpha$  denotes the index of the horizontal, vertical derivative domain and intensity domain,  $f(\alpha)$  denotes the fractal dimension respectively.

$$SPCR_{scharr}(I) = \bigcup_i d_{DBC}(P_i(PC_{scharr}(m(I)))), \quad (13)$$

where  $P_i$  denotes the operator that extracts the  $i$ th sub-image and  $\bigcup$  denotes the concatenation of all the values into a vector. In the rest of this paper, we refer SPCR feature as the modified version.

#### 4.2. Similarity index of PC regularity

Once the SPCR features of the perfect image  $I_p$  and the distorted image  $I_d$  have been obtained, we compute our SPCR measure (SPCRM) by calculating the  $\ell_1$  distance of the two feature vectors as follows:

$$SPCRM_{int}(I_p, I_d) = \|SPCR_{int}(I_p) - SPCR_{int}(I_d)\|_1, \quad (14)$$

$$SPCRM_{scharr}(I_p, I_d) = \|SPCR_{scharr}(I_p) - SPCR_{scharr}(I_d)\|_1. \quad (15)$$

Due to the nature of the SPCR feature, the SPCRM value measures the difference between the distorted image and

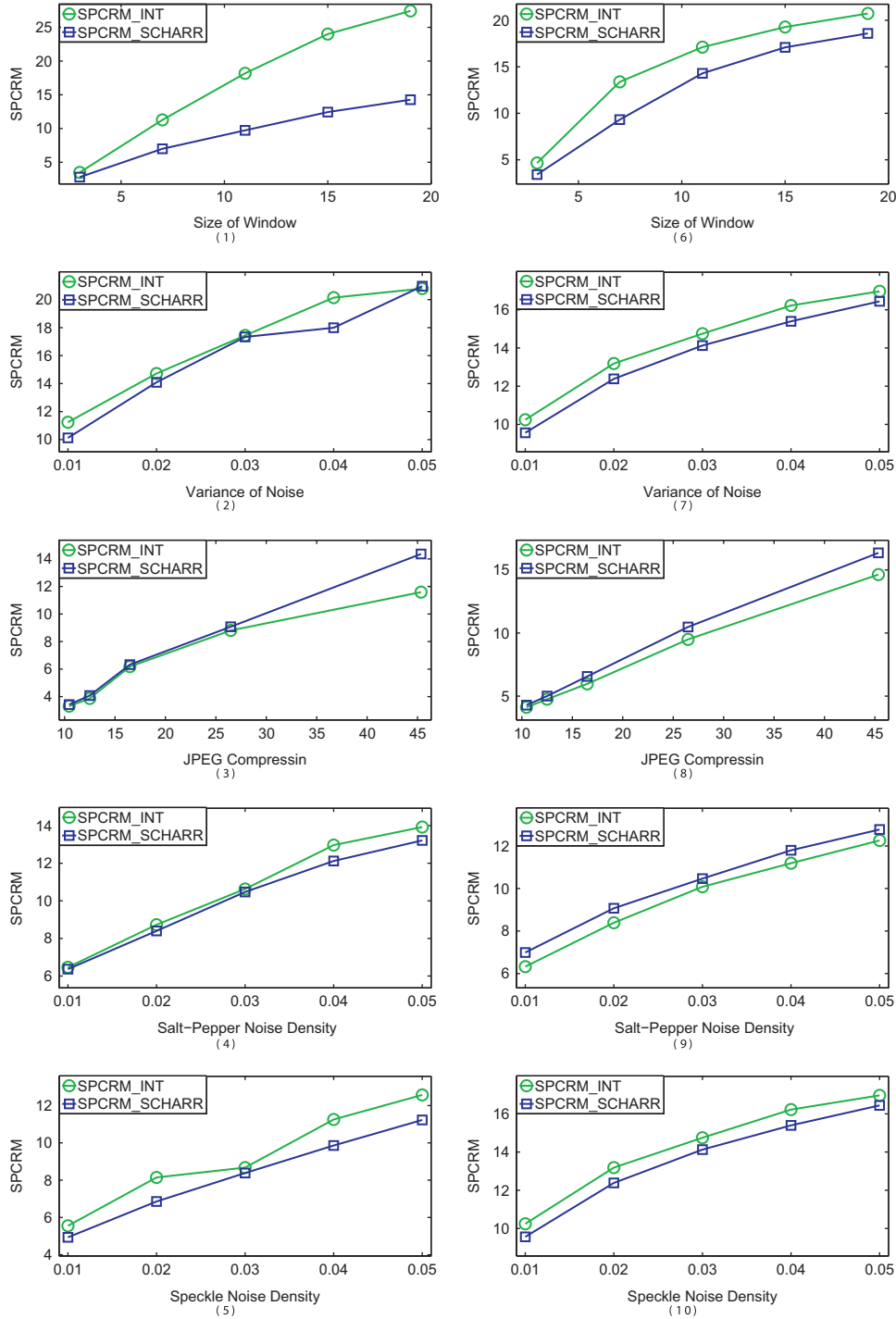


**Fig. 5.** Rationality and Sensitivity of SPCRM, (1)–(5) SPCRM of reference image in Fig. 3 with blurred, Gaussian noise contaminated, JPEG compressed, salt-pepper noise contaminated and speckle noise contaminated; (6)–(10) Average SPCRM of reference images in LIVE with blurred, Gaussian noise contaminated, JPEG compressed, salt-pepper noise contaminated and speckle noise contaminated.

the perfect image in the meaning of the regularity of the local spatial distribution of the image structures.

To verify the effectiveness of the SPCRM, we compute the SPCRM of the reference image in Fig. 3 with different distortions, which are blurring (with smoothing window),

additive Gaussian noise (with zero-mean and the changing variance), JPEG compression (with the changing compression rate), salt-pepper noise (with the changing density), and speckle noise (with the changing density). Fig. 5(1–5) shows the reference images with different types of

**Table 2**

Details of seven benchmark databases.

Database	Reference img	Distorted img	Distortion types
TID2008	25	1700	17
CSIQ	30	866	6
LIVE	29	779	5
IVC	10	185	4
MIC	14	168	2
WIQ	7	80	1
A57	3	54	6

distortions and the metric prediction trends to the corresponding image, respectively. In the light of the fact that an IQA metric can be viewed as a excellent metric as long as the metric monotonously changes with distortion increasing. Moreover, from Fig. 5, it is found that the proposed framework prediction trends to rise when the degree of the distortion is increasing. It is consistent well with the tendency of the decreasing image quality in fact. So the results demonstrate the rationality of the proposed framework. We do the same experiment using the 29 original images in the LIVE database. The average of all SPCRM is shown in Fig. 5(6–10), which gives a similar conclusion.

## 5. Experiment

### 5.1. Benchmark datasets and test methodology

There are seven public benchmark databases widely used in the IQA community, including the TID2008 database [42], the CSIQ database [43], the LIVE database [41], the IVC database [44], the MIC database [45], the WIQ database [46] and the Cornell\_A57 database [47]. All of them are used for the evaluation of our method. The important information of these seven databases, in terms of the number of reference images, the number of distorted images, and the number of quality distortion types is summarized in Table 2.

For quantifying the performance of our approach, we employ five popular criteria, including the Pearson linear correlation coefficient (PLCC), the Spearman rank-order correlation coefficient (SROCC), the Kendall rank-order correlation coefficient (KROCC), the root mean square error (RMSE) and the mean absolute error (MAE). The PLCC, RMSE and MAE metrics are used to measure the prediction accuracy, while the SROCC and KROCC metrics are used to measure the monotonicity. These performance criteria except KROCC are recommended by video quality experts group [48]. A desirable objective RR-IQA measure is expected to have high values of the SROCC, KROCC and PLCC metrics, and meanwhile have low values of the RMSE and MAE metrics. Before computing all the metrics, a regression analysis is required to provide a nonlinear mapping between the objective scores and the subjective mean opinion scores (MOS). In our setting, we used the following mapping function [49], which is a logistic function with an added linear term, constrained to be

**Table 3**

SROCC values vs the size of image on CSIQ database.

Database	512 × 512	256 × 256	128 × 128
CSIQ	0.8110	0.9410	0.8909

monotonic,

$$f(x) = \beta_1 \left( \frac{1}{2} - \frac{1}{1 + \exp(\beta_2(x - \beta_3))} \right) + \beta_4 x + \beta_5, \quad (16)$$

where  $\beta_i, i = 1, 2, \dots, 5$  are the parameters to be fitted by logistic regression, which are determined by minimizing the sum of squared differences between the mapped objective scores and the subjective ratings.

For evaluating the performance of our approach, we compare our approach with four representative and competitive RR-IQA metrics, including the WNISM [3], the HWD2 [10], the RR-SSIM [2] and the RRED [13]. Furthermore, we also compare our RR-IQA method with five FR-IQA approaches, including the FSIM [6], the IW-SSIM [50], the VIF [4], the SSIM [29] and the PSNR. Not all of these approaches have been evaluated for all the datasets we use. We only refer the results that are available. To further understand the behavior of our RR-IQA approach, we also compare the performance of our SPCRM method on three largest databases (TID2008, CSIQ and LIVE) with respect to each image distortion type.

### 5.2. Implementation of SPCRM

It should be noted that the SPCRM will be most effective if used on the appropriate scale, while it depends on both the image resolution and the viewing distance and hence is difficult to be obtained. In our implementation, we follow the empirical scale proposed by [51] and normalized all the images to  $256 \times 256$ . In Table 3, We compare the SROCC scores with non-normalization and normalization (normalized to  $256 \times 256$  and normalized to  $128 \times 128$ ) on the CSIQ database whose raw image size is  $512 \times 512$ , one can clearly see that empirical scale does effect the performance of proposed approach. After normalization, SPCRM uses less data of the reference image and achieves higher prediction accuracy.

The block size is one parameter in the proposed SPCRM approach, which is used to compute block-wise DBC fractal dimension and also determines the feature length. In the literature, two strategies are often used in the parameterization process. One is to choose the parameters depending on how well the resulting model fits the physiological or psychophysical data, e.g. [10]. The other strategy is to train the parameters to optimize performance in terms of predicting subjective ratings, e.g. [6]. We adopt the second strategy. More precisely, we tuned the parameter based on TID2008, CSIQ and LIVE databases. Fig. 6 shows the performance of our method with respect to different sizes of block. As we can see, the performance of SPCRM\_SCHARR increases as the size of blocks decreases, while SPCRM\_INT is relatively stable.

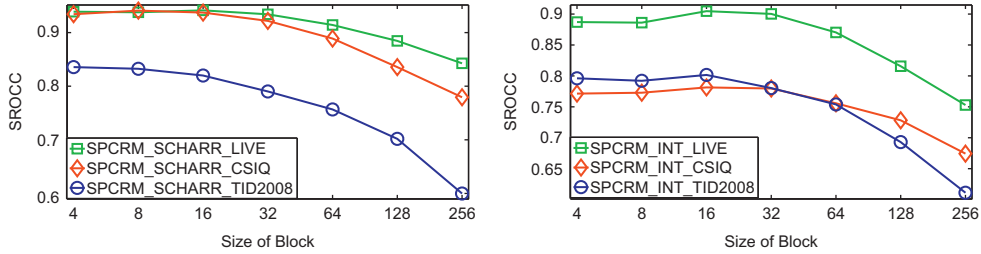


Fig. 6. The performance of SPCRM in terms of SROCC vs. size of block on the three databases (TID2008, CSIQ and LIVE).

Table 4

SROCC values using three gradient operators.

Database	Scharr	Sobel	Prewitt
LIVE	0.9444	0.9439	0.9441

In our proposed metrics SPCRM, the gradient needs to be calculated. To this end, three commonly used gradient operators listed in Table 1 are examined. The selection criterion is that the gradient operator leading to a higher SROCC would be selected. The SROCC values obtained by the three gradient operators on the LIVE database are listed in Table 4, from which we can see that the Scharr operator could achieve slightly better performance than the other two. Thus, in all of the following experiments, the Scharr operator is used to calculate the gradient in SPCRM.

### 5.3. Performance comparison

The experimental results of the proposed SPCRM and the compared approaches on seven benchmark databases are listed in Table 5. The FR-IQA indices which perform the best on each database are marked in boldface and RR-IQA indices are marked underlined. To provide an overall indication of the comparative performance of the different schemes, Table 5 also gives the average PLCC, SROCC, and KROCC results over seven databases, where the average values are computed in two cases [2]. In the first case, the correlation scores are directly averaged, whereas in the second case, different weights are assigned to the databases depending on the number of the distorted images in each database (refer to Table 2).

From Table 5 it can be seen that the proposed SPCRM\_SCHARR approach outperforms other RR-IQA methods on all databases except some evaluation criteria on LIVE database. In order to further demonstrate the effectiveness of the proposed metric, SPCRM\_SCHARR is also compared with the overall indication of the FR-IQA schemes, one can see that the SPCRM\_SCHARR performs the best or close to the best on average no matter what kind of averaging is used and what the evaluation criterion is. This further confirms that the proposed RR-IQA metric outperforms the state-of-the-art RR-IQA metrics.

For visualization, we show the scatter plots of predicted quality scores against subjective DMOS scores for two

representative RR-IQA models (RRED and WNISM) on the CSIQ database, which has six types of distortions (AWN, JPEG, JPEG2000, PGN, GB and CTD) in Fig. 7. One can observe that for SPCRM\_INT, the distribution of predicted scores on the CTD distortion deviates much from the distributions on other types of distortions, degrading its overall performance. Tables 5 and 6 show that WNISM performs well on the single distortion type but not very well on the whole databases. This is mainly because WNISM does not predict the image's quality consistently across different distortion types on entire database, as can also be observed from the scatter plots with CSIQ database in Fig. 7.

### 5.4. Performance comparison on individual distortion types

Good overall performance does not necessarily mean good performance for individual distortion types. To examine how the proposed SPCRM method behaves on different distortion types, we show the performance of the SPCR features on each type of the TID2008, CSIQ and LIVE databases in Table 6. For easier comparison, only the SROCC values are listed. SROCC is chosen because it is suitable for measuring a small number of data points and its value will not be affected by an unsuccessful monotonic nonlinear mapping. There are a total of 28 groups of distorted images in the three databases. We use boldface font to highlight the best model in each group. One can see that RRED is marked 19 times, followed by SPCRM\_SCHARR, which is only 8 times. However, SPCRM\_SCHARR is better than RRED in terms of overall performance on the three databases.

Generally speaking, performing well on specific types of distortions does not guarantee that an IQA model will perform well on the whole database with a broad spectrum of distortion types. A good IQA model should also predict the image quality consistently across different types of distortions. Referring to the scatter plots in Fig. 7, it can be seen that the scatter plot of SPCRM\_SCHARR is more concentrated across different groups of distortion types. For example, its points corresponding to JPEG, PGN and CTD distortions are very close to each other. However, the points corresponding to JPEG, PGN and CTD for RRED are relatively far from each other. This explains why some RR-IQA models perform well for many individual types of distortions but they do not perform well on the entire databases; that is, these IQA models behave rather differently on different types of



**Table 5**  
Performance comparison on seven benchmark databases (img.size\* is the image size after normalization).

Database Type	Criteria	SPCRM-SCHARR RR	SPCRM-INT RR	RRED [13] RR	SPCRM-SCHARR RR	SPCRM-INT RR	RR-SSIM [2] RR	HWD2 [10] RR	WNISM [3] RR	FSIM [6] FR	IW-SSIM [50] FR	VIF [4] FR	SSIM [29] FR	PSNR FR
Length		img.size*/32	img.size*/64	img.size/36	32	16	36	18	16	img.size	img.size	img.size	img.size	img.size
TID 2008	PLCC	<b>0.8509</b>	0.8132	0.8255	0.7403	0.7560	0.7231	N/A	0.5891	<b>0.8738</b>	0.8579	0.8084	0.7732	0.5734
	SROCC	<b>0.8325</b>	0.7921	0.8237	0.7567	0.7539	0.7231	N/A	0.5119	<b>0.8805</b>	0.8559	0.7491	0.7749	0.5531
	KROCC	<b>0.6448</b>	0.5967	0.6346	0.5506	0.5500	0.7231	N/A	0.3589	<b>0.6946</b>	0.6636	0.5860	0.5768	0.4027
	RMSE	<b>0.7050</b>	0.7809	0.7573	0.9021	0.8784	0.7231	N/A	1.0843	<b>0.6525</b>	0.6895	0.7899	0.8511	1.0994
	MAE	<b>0.5434</b>	0.6099	0.5641	0.6979	0.6902	0.7231	N/A	0.8666	<b>0.4926</b>	0.5276	0.6000	0.6547	0.8327
CSIQ	PLCC	<b>0.9464</b>	0.8341	0.9121	0.8906	0.8076	0.8426	N/A	0.7124	0.9120	0.9144	<b>0.9277</b>	0.8613	0.8000
	SROCC	<b>0.9410</b>	0.7728	0.9184	0.8889	0.7557	0.8527	N/A	0.7431	0.9242	0.9213	<b>0.9195</b>	0.8756	0.8058
	KROCC	<b>0.7848</b>	0.5894	0.7429	0.7097	0.5663	0.6540	N/A	0.5457	0.7567	0.7529	<b>0.7537</b>	0.6907	0.6084
	RMSE	<b>0.0848</b>	0.1448	0.1077	0.1194	0.1548	0.1413	N/A	0.1842	0.1077	0.1063	<b>0.0980</b>	0.1334	0.1575
	MAE	<b>0.0659</b>	0.1162	0.0820	0.0902	0.1240	0.1092	N/A	0.1492	0.0797	0.0801	<b>0.0743</b>	0.0991	0.1195
LIVE	PLCC	0.9412	0.8871	0.9385	0.9097	0.8733	0.9194	<b>0.9624</b>	0.7365	0.9597	0.9522	<b>0.9604</b>	0.9449	0.8723
	SROCC	<b>0.9444</b>	0.8886	0.9429	0.9131	0.8732	0.9129	0.9418	0.7472	0.9634	0.9567	<b>0.9636</b>	0.9479	0.8756
	KROCC	<b>0.7909</b>	0.7020	0.7888	0.7392	0.6831	0.7349	N/A	0.5577	<b>0.8337</b>	0.8175	0.8282	0.7963	0.6865
	RMSE	9.2300	12.6094	9.4317	11.3450	13.3087	11.3026	<b>6.3657</b>	18.4814	7.6780	8.3473	<b>7.6137</b>	8.9455	13.3597
	MAE	7.1328	9.9588	7.2976	8.7882	10.3555	9.1889	<b>4.8445</b>	14.6352	<b>5.9468</b>	6.4702	6.1070	6.9325	10.5093
IVC	PLCC	<b>0.9294</b>	0.8449	0.9050	0.8252	0.7080	0.8177	N/A	0.5311	<b>0.9376</b>	0.9231	0.9028	0.9119	0.7196
	SROCC	<b>0.9225</b>	0.8447	0.8987	0.8186	0.7018	0.8154	N/A	0.4114	<b>0.9262</b>	0.9125	0.8964	0.9018	0.6884
	KROCC	<b>0.7530</b>	0.6501	0.7175	0.6256	0.5121	0.6164	N/A	0.2907	<b>0.7564</b>	0.7339	0.7158	0.7223	0.5218
	RMSE	<b>0.4498</b>	0.6518	0.5183	0.6881	0.8604	0.7014	N/A	1.0322	<b>0.4236</b>	0.4686	0.5239	0.4999	0.8460
	MAE	<b>0.3542</b>	0.5192	0.3971	0.5188	0.6997	0.5619	N/A	0.8550	<b>0.3388</b>	0.3694	0.4104	0.3777	0.6677
MIST	PLCC	<b>0.8885</b>	0.8166	0.8272	0.7954	0.6541	0.8051	N/A	0.6542	0.9078	<b>0.9248</b>	0.9138	0.8887	0.6429
	SROCC	<b>0.8831</b>	0.8054	0.8228	0.8074	0.6475	0.8003	N/A	0.6322	0.9059	<b>0.9202</b>	0.9077	0.8794	0.6132
	KROCC	<b>0.6997</b>	0.6116	0.6306	0.6099	0.4673	0.6090	N/A	0.4570	0.7302	<b>0.7537</b>	0.7315	0.6939	0.4443
	RMSE	<b>0.5742</b>	0.7224	0.7033	0.7586	0.9466	0.7423	N/A	0.9464	0.5248	<b>0.4761</b>	0.5084	0.5738	0.9585
	MAE	<b>0.4352</b>	0.5436	0.5465	0.6269	0.7432	0.5648	N/A	0.7742	0.4021	<b>0.3677</b>	0.4038	0.4386	0.7761
A57	PLCC	<b>0.9478</b>	0.8813	0.8547	0.6558	0.8282	0.7044	N/A	0.5125	<b>0.9393</b>	0.9034	0.6915	0.8017	0.7073
	SROCC	<b>0.9398</b>	0.8627	0.8399	0.6538	0.7839	0.7301	N/A	0.3140	<b>0.9181</b>	0.8709	0.6223	0.8066	0.6189
	KROCC	<b>0.8077</b>	0.6902	0.6483	0.4818	0.5825	0.5345	N/A	0.2210	<b>0.7639</b>	0.6842	0.4589	0.6058	0.4309
	RMSE	<b>0.0784</b>	0.1162	0.1276	0.1856	0.1377	0.1744	N/A	0.2317	<b>0.0844</b>	0.1054	0.1784	0.1469	0.1737
	MAE	<b>0.0597</b>	0.0900	0.1051	0.1457	0.1041	0.1433	N/A	0.1971	<b>0.0721</b>	0.0892	0.1329	0.1209	0.1417
WIQ	PLCC	<b>0.8954</b>	0.8781	0.8367	0.7933	0.7943	N/A	N/A	0.3401	<b>0.8546</b>	0.8329	0.7605	0.7980	0.7939
	SROCC	<b>0.8846</b>	0.8587	0.7626	0.7500	0.7769	N/A	N/A	0.2156	<b>0.8006</b>	0.7865	0.6918	0.7261	0.6257
	KROCC	<b>0.7146</b>	0.6728	0.5864	0.5689	0.5702	N/A	N/A	0.1561	<b>0.6215</b>	0.6038	0.5246	0.5569	0.4626
	RMSE	<b>10.1981</b>	10.9614	12.5448	13.9473	13.9160	N/A	N/A	21.5404	<b>11.8949</b>	12.6765	14.8731	13.8046	14.1381
	MAE	<b>7.7062</b>	8.6875	9.8095	11.1770	11.3315	N/A	N/A	16.9682	<b>9.0496</b>	9.9121	12.2465	10.9873	11.2027
Weighted Average	PLCC	<b>0.8986</b>	0.8369	0.8714	0.8151	0.7865	0.7995	N/A	0.6407	<b>0.9050</b>	0.8960	0.8728	0.8407	0.7020
	SROCC	<b>0.8889</b>	0.8129	0.8584	0.8220	0.7723	0.7996	N/A	0.6034	<b>0.9094</b>	0.8955	0.8423	0.8430	0.6874
	KROCC	<b>0.7175</b>	0.6226	0.6784	0.6305	0.5762	0.6061	N/A	0.4364	<b>0.7409</b>	0.7215	0.6827	0.6593	0.5161
Direct Average	PLCC	<b>0.9142</b>	0.8508	0.8714	0.8015	0.7745	0.8021	N/A	0.5823	<b>0.9121</b>	0.8542	0.8522	0.8542	0.7299
	SROCC	<b>0.9068</b>	0.8321	0.8584	0.7984	0.7561	0.8054	N/A	0.5108	<b>0.9027</b>	0.8446	0.8215	0.8446	0.6830
	KROCC	<b>0.7422</b>	0.6447	0.6784	0.6122	0.5616	0.6121	N/A	0.3696	<b>0.7367</b>	0.6632	0.6570	0.6632	0.5082

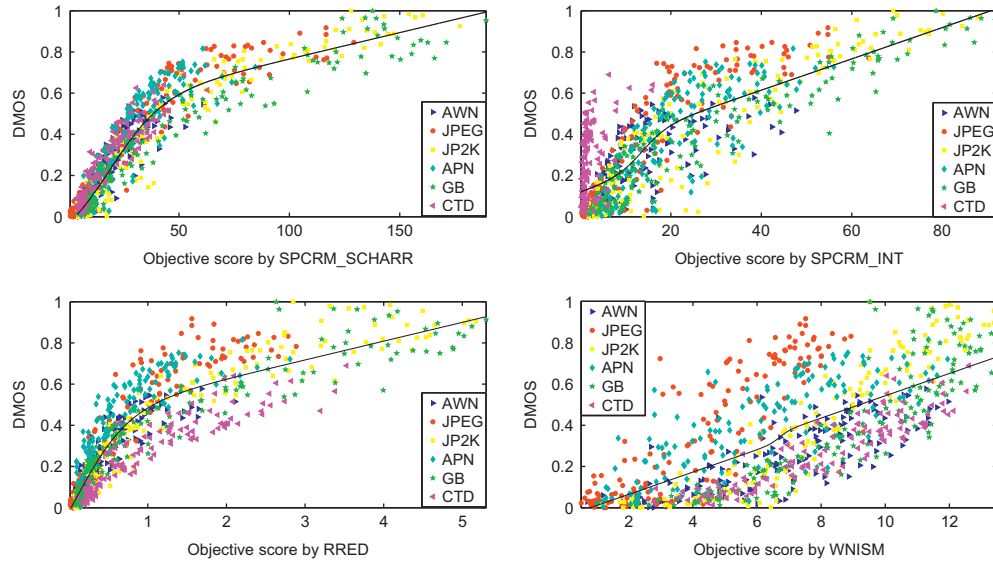


**Fig. 7.** Scatter plots of predicted quality scores against the subjective quality scores (DMOS) by representative RR-IQA models on the CSIQ database. The six types of distortions are represented by different shaped colors.

**Table 6**

Performance of SPCRM with respect to individual distortion type on the TID2008, CSIQ, and LIVE databases (img.size\* is the image size after normalization).

Database	Distortion type	SPCRM-SCHARR img.size*/32	SPCRM-INT img.size*/64	RRED [13] img.size/36	SPCRM-SCHARR 32	SPCRM-INT 16	RR-SSIM [2] 36	HWD2 [10] 16	WNISM [3] 18
Length									
TID2008	Additive Gaussian noise	0.8145	0.6717	<b>0.8203</b>	0.6294	0.6385	N/A	N/A	0.6037
	Noise in color comp.	0.7995	0.6225	<b>0.8502</b>	0.6189	0.5496	N/A	N/A	0.6076
	Spatially corr. noise	0.8296	0.6957	<b>0.8417</b>	0.6546	0.6396	N/A	N/A	0.6008
	Masked noise	0.7601	0.5865	<b>0.8325</b>	0.6336	0.5734	N/A	N/A	0.6311
	High frequency noise	0.8826	0.7925	<b>0.9088</b>	0.7749	0.7882	N/A	N/A	0.7064
	Impulse noise	0.6755	0.5560	<b>0.7407</b>	0.5598	0.5943	N/A	N/A	0.5922
	Quantization noise	<b>0.8551</b>	0.7895	0.8308	0.7435	0.7608	N/A	N/A	0.6096
	Gaussian blur	0.9195	0.8784	<b>0.9573</b>	0.8714	0.8386	N/A	N/A	0.8723
	Image denoising	0.9480	0.9133	<b>0.9493</b>	0.8746	0.8823	N/A	N/A	0.8582
	JPEG compression	0.9166	0.8807	<b>0.9333</b>	0.8729	0.8231	N/A	N/A	0.8246
	JPEG2000 compression	0.9592	0.9480	<b>0.9681</b>	0.9298	0.9204	N/A	N/A	0.9344
	JPEG trans. error	<b>0.8867</b>	0.8525	0.8704	0.8689	0.8023	N/A	N/A	0.8774
	JPEG2000 trans. error	<b>0.8476</b>	0.7602	0.7421	0.7880	0.7247	N/A	N/A	0.6889
	Non ecc. patt. noise	<b>0.8190</b>	0.8423	0.7127	0.6693	0.6781	N/A	N/A	0.4293
	Local block-wise dist.	0.8489	0.7533	<b>0.8243</b>	0.7811	0.6519	N/A	N/A	0.6071
	Mean shift	<b>0.7144</b>	0.4331	0.5378	0.7478	0.4769	N/A	N/A	0.3204
	Contrast change	0.0759	<b>0.5903</b>	0.5424	0.3148	0.5699	N/A	N/A	0.7042
CSIQ	Additive Gaussian noise	0.9193	0.7645	<b>0.9353</b>	0.8137	0.7760	N/A	N/A	0.8188
	JPEG compression	<b>0.9555</b>	0.9238	0.9521	0.9179	0.9089	N/A	N/A	0.8955
	JPEG2000 compression	0.9578	0.9086	<b>0.9628</b>	0.8820	0.8873	N/A	N/A	0.9405
	Additive pink noise	0.9232	0.8193	<b>0.9362</b>	0.8423	0.7952	N/A	N/A	0.8002
	Gaussian blur	<b>0.9690</b>	0.9399	0.9634	0.9530	0.9314	N/A	N/A	0.9144
LIVE	Contrast change	0.9238	0.4443	<b>0.9383</b>	0.9014	0.4245	N/A	N/A	0.9122
	JPEG2000 compression	0.9568	0.9023	<b>0.9580</b>	0.9273	0.8960	N/A	0.9362	0.9330
	JPEG compression	0.9747	0.9328	<b>0.9760</b>	0.9444	0.9217	N/A	0.9543	0.9204
	Additive Gaussian noise	<b>0.9734</b>	0.9213	0.9678	0.9273	0.9341	0.9642	0.9321	0.8701
	Gaussian blur	0.9590	0.9172	<b>0.967</b>	0.9401	0.9022	0.8692	0.8282	0.9145
	JPEG2000 trans. error	0.9277	0.9050	<b>0.9427</b>	0.8861	0.8936	0.9137	0.9386	0.9227

distortions, which can be attributed to the different ranges of quality scores for those distortion types.

Furthermore, it should be noted that the SPCRM has some difficulty in predicting the quality of the images with

distortions caused by mean value shift or contrast change. The reason is that PC is dimensionless measure and is independent of the image illumination or contrast as discussed in Section 3.1.

**Table 7**

Time cost of each metric.

Model Type	SPCRM_SCHARR RR	SPCRM_INT RR	RRED [13] RR	RR-SSIM [2] RR	HWD2 [10] RR	WNISM [3] RR	FSIM [6] FR	IW-SSIM [50] FR	VIF [4] FR	SSIM [29] FR	PSNR FR
Time (s)	3.05	1.53	2.86	N/A	N/A	6.49	1.89	2.24	5.16	0.13	0.01

### 5.5. Evaluation of running speed

We also evaluate the running speed of each selected IQA index. The test is performed on a Dell Inspiron INSP1440 PC embedded with an Intel T6600 processor and 2GB RAM. The software platform is Matlab R2011b. The size of the test image is  $768 \times 512$ . All the MATLAB source codes were obtained from the original authors. Table 7 shows the running time of the 11 IQA models. Clearly, SPCRM\_INT is much faster than WNISM, RRED, SPCRM\_SCHARR and RR-SSIM (according to [2], WNISM is about 2 times faster than RR-SSIM), SPCRM\_SCHARR approach is about the same time as the RRED approach and about half time as the WNISM approach. More precisely, the huge complexity of WNISM, RRED and RR-SSIM mainly comes from the highly overcomplete steerable pyramid decomposition. Computation of PC is the main reason for the complexity of SPCRM. According to Table 7, the computational complexity of our approach is acceptable.

## 6. Conclusion

Since the quality of an image depends not only on the content of the image but also on the perception ability of human. Based on the fact that visually discernable features coincide with those points where the Fourier waves at different frequencies have congruent phases. In this paper, we have proposed a new RR-IQA scheme based on PC.

For characterizing the distortion of image content, many traditional reduced reference image quality assessment approaches are proposed based on counting and comparing the numbers of local elements of the reference image and the distorted image. Such approaches may lose the details of the spatial distribution of the image elements. To overcome this problem, the regularity of spatial arrangement is accounted in this paper. Fractal analysis is employed to characterize the difference of the PC distributions in intensity and partial derivative domain between the reference image and the distorted image.

To demonstrate the power of the proposed approach, seven public benchmark databases and five performance metrics are involved for evaluation. Our approach performs on a par with other state-of-the-art approaches. In the future, we will study the application of our approach to video quality assessment.

## References

- [1] Z. Wang, A. Bovik, *Modern Image Quality Assessment*, Morgan & Claypool Publishers, 2006.
- [2] A. Rehman, Z. Wang, Reduced-reference image quality assessment by structural similarity estimation, *IEEE Trans. Image Process.* 21 (8) (2012) 3378–3389.
- [3] Z. Wang, G. Wu, H.R. Sheikh, E.P. Simoncelli, E.H. Yang, A.C. Bovik, Quality-aware images, *IEEE Trans. Image Process.* 15 (6) (2006) 1680–1689.
- [4] H.R. Sheikh, A.C. Bovik, Image information and visual quality, *IEEE Trans. Image Process.* 15 (2) (2006) 430–444.
- [5] N. Damera-Venkata, T.D. Kite, W.S. Geisler, B.L. Evans, A.C. Bovik, Image quality assessment based on a degradation model, *IEEE Trans. Image Process.* 9 (4) (2000) 636–650.
- [6] L. Zhang, L. Zhang, X.Q. Mou, D. Zhang, FSIM: a feature similarity index for image quality assessment, *IEEE Trans. Image Process.* 20 (8) (2011) 2378–2386.
- [7] H.R. Sheikh, A.C. Bovik, L.K. Cormack, No-reference quality assessment using natural scene statistics: JPEG2000, *IEEE Trans. Image Process.* 14 (11) (2005) 1918–1927.
- [8] Z. Wang, A.C. Bovik, B.L. Evans, Blind measurement of blocking artifacts in images, in: *Proceedings of IEEE International Conference Image Processing*, vol. 3, 2000, pp. 981–984.
- [9] Z. Wang, H.R. Sheikh, A.C. Bovik, No-reference perceptual quality assessment of JPEG compressed images, in: *Proceedings of IEEE International Conference Image Processing*, vol. 1, 2002, pp. 477–480.
- [10] X. Gao, W. Lu, D. Tao, X. Li, Image quality assessment based on multiscale geometric analysis, *IEEE Trans. Image Process.* 18 (7) (2009) 1409–1423.
- [11] U. Engelke, M. Kusuma, H.J. Zepernick, M. Caldera, Reduced-reference metric design for objective perceptual quality assessment in wireless imaging, *Signal Process. Image Commun.* 24 (7) (2009) 525–547.
- [12] Q. Li, Z. Wang, Reduced-reference image quality assessment using divisive normalization-based image representation, *IEEE J. Sel. Top. Signal Process.* 3 (2) (2009) 202–211 (special issue on Visual Media Quality Assessment).
- [13] R. Soundararajan, A.C. Bovik, RRED indices: Reduced reference entropic differencing for image quality assessment, *IEEE Trans. Image Process.* 21 (2) (2012) 517–526.
- [14] Z. Wang, E.P. Simoncelli, Reduced-reference image quality assessment using a wavelet-domain natural image statistic model, in: *Human Vision and Electronic Imaging X*, Proc. SPIE, San Jose, CA, vol. 5666, 2005, pp. 149–159.
- [15] W.F. Xue, X.Q. Mou, Reduced reference image quality assessment based on Weibull statistics, in: *Proceedings of the International Workshop on Quality of Multimedia Experience*, 2010, pp. 1–6.
- [16] L. Ma, S.N. Li, F. Zhang, K.N. Ngan, Reduced-reference image quality assessment using reorganized DCT-based image representation, *IEEE Trans. Multimed.* 13 (3).
- [17] A.A. Abdelouahad, M.E. Hassouni, H. Cherifi, D. Aboutajdine, Image quality assessment based on IMF coefficients modeling, in: *Proceedings of the International Conference on Digital Information and Communication Technology and its Applications*, 2011, pp. 131–145.
- [18] I.P. Gunawanand, M. Ghanbari, Reduced reference picture quality estimation by using local Harmonic amplitude information, in: *Proceedings of London Communications Symposium*, 2003, pp. 137–140.
- [19] M. Morrone, J. Ross, D. Burr, R. Owens, Mach bands are phase dependent, *Nature* 324 (6094) (1986) 250–253.
- [20] M. Morrone, R. Owens, Feature detection from local energy, *Pattern Recognit. Lett.* 6 (5) (1987) 303–313.
- [21] M. Morrone, D. Burr, Feature detection in human vision: a phase-dependent energy model, *Proc. R. Soc. Lond. B Biol. Sci.* (1988) 221–245.
- [22] P. Kovessi, Image features from phase congruency, *Videre: J. Comput. Vis. Res.* 1 (3) (1999) 1–26.
- [23] L. Henriksson, A. Hyvärinen, S. Vanni, Representation of cross-frequency spatial phase relationships in human visual cortex, *J. Neurosci.* 29 (45) (2009) 14342–14351.
- [24] A. Saha, Q. Jonathan Wu, Perceptual image quality assessment using phase deviation sensitive energy features, *Signal Process.* 93 (11) (2013) 3182–3191.

- [25] Z. Liu, R. Laganière, Phase congruence measurement for image similarity assessment, *Pattern Recognit. Lett.* 28 (1) (2007) 166–172.
- [26] C. Li, A. Bovik, X. Wu, Blind image quality assessment using a general regression neural network, *IEEE Trans. Neural Netw.* 22 (5) (2011) 793–799.
- [27] R. Hassen, Z. Wang, M. Salama, No-reference image sharpness assessment based on local phase coherence measurement, in: 2010 IEEE International Conference on Acoustics Speech and Signal Processing (ICASSP), 2010, pp. 2434–2437.
- [28] T.M. Kusuma, H.J. Zepernick, A reduced-reference perceptual quality metric for inservice image quality assessment, in: Proceedings of Workshop on Mobile Future and Symposium on Trends in Communications, 2003, pp. 71–74.
- [29] Z. Wang, A.C. Bovik, H.R. Sheikh, E.P. Simoncelli, Image quality assessment: from error visibility to structural similarity, *IEEE Trans. Image Process.* 13 (4) (2004) 600–612.
- [30] Y. Xu, H. Ji, C. Fermüller, Viewpoint invariant texture description using fractal analysis, *Int. J. Comput. Vis.* 83 (1) (2009) 85–100.
- [31] A. Oppenheim, J. Lim, The importance of phase in signals, *Proc. IEEE* 69 (5) (1981) 529–541.
- [32] P. Kovcs, A dimensionless measure of edge significance from phase congruency calculated via wavelets, in: First New Zealand Conference on Image and Vision Computing, 1993, pp. 87–94.
- [33] B.B. Mandelbrot, *The Fractal Geometry of Nature*, Freeman, San Francisco, CA, 1982.
- [34] N. Sarkar, B.B. Chaudhuri, An efficient differential box-counting approach to compute fractal dimension of image, *IEEE Trans. Syst. Man Cybernet.* 24 (1) (1994) 115–120.
- [35] S.S. Chen, Fractal geometry in image understanding (Ph.D. dissertation), University of Missouri-Columbia, 1987.
- [36] A.S. Balghonaim, J.M. Keller, A maximum likelihood estimate for two-variable fractal surface, *IEEE Trans. Image Process.* 7 (12) (1997) 1746–1753.
- [37] A.P. Pentland, Fractal-based description of natural scenes, *IEEE Trans. Pattern Anal. Mach. Intell.* 6 (6) (1984) 661–674.
- [38] A. Liu, W. Lin, M. Narwaria, Image quality assessment based on gradient similarity, *IEEE Trans. Image Process.* 21 (4) (2012) 1500–1512.
- [39] G.-H. Chen, C.-L. Yang, S.-L. Xie, Gradient-based structural similarity for image quality assessment, in: 2006 IEEE International Conference on Image Processing, 2006, pp. 2929–2932.
- [40] D.-O. Kim, H.-S. Han, R.-H. Park, Gradient information-based image quality metric, *IEEE Trans. Consum. Electron.* 56 (2) (2010) 930–936.
- [41] H.R. Sheikh, K. Seshadrinathan, A.K. Moorthy, Z. Wang, A.C. Bovik, L. K. Cormack, Image and video quality assessment research at LIVE, (<http://live.ece.utexas.edu/research/quality>).
- [42] N. Ponomarenko, V. Lukin, A. Zelensky, K. Egiazarian, M. Carli, F. Battisti, TID2008 - a database for evaluation of full-reference visual quality assessment metrics, *Adv. Modern Radioelectron.* 10 (10) (2009) 30–45.
- [43] E.C. Larson, D.M. Chandler, Categorical Image Quality (CSIQ) Database, (<http://vision.okstate.edu/csiq>).
- [44] A. Ninassi, P.L. Callet, F. Autrusseau, Subjective quality assessment-IVC database, (<http://www2.irccyn.ec-nantes.fr/ivcdb>).
- [45] Y. Horita, K. Shibata, Y. Kawayoke, Z.M.P. Sazzad, MICT image quality evaluation database, (<http://mict.eng.u-toyama.ac.jp/mict/index2.html>).
- [46] U. Engelke, H.J. Zepernick, M. Kusuma, Wireless imaging quality database, (<http://www.bth.se/tek/rcg.nsf/pages/wiq-db>) (2010).
- [47] D.M. Chandler, S.S. Hemami, A57 database, (<http://foulard.ece.conell.edu/dmc27/vsnr/vsnr.html>).
- [48] VQEG, Final report from the video quality experts group on the validation of objective models of video quality assessment, (<http://www.vqeg.org>), 2000.
- [49] H.R. Sheikh, M.F. Sabir, A.C. Bovik, A statistical evaluation of recent full reference image quality assessment algorithms, *IEEE Trans. Image Process.* 15 (11) (2006) 3440–3451.
- [50] Z. Wang, Q. Li, Information content weighting for perceptual image quality assessment, *IEEE Trans. Image Process.* 20 (5) (2011) 1185–1198.
- [51] Z. Wang, SSIM Index for image quality assessment, (<https://ece.uwaterloo.ca/%7Ez70wang/research/ssim/>).